ADVANCED MATERIALS
www.advmat.de

Identifying Ionic and Electronic Charge Transfer at Oxide Heterointerfaces

Marc-André Rose, Břetislav Šmíd, Mykhailo Vorokhta, Ivetta Slipukhina, Michael Andrä, Hendrik Bluhm, Tomáš Duchoň, Marjana Ležaić, Scott A. Chambers, Regina Dittmann, David N. Mueller,* and Felix Gunkel**

The ability to tailor oxide heterointerfaces has led to novel properties in low-dimensional oxide systems. A fundamental understanding of these properties is based on the concept of electronic charge transfer. However, the electronic properties of oxide heterointerfaces crucially depend on their ionic constitution and defect structure: ionic charges contribute to charge transfer and screening at oxide interfaces, triggering a thermodynamic balance of ionic and electronic structures. Quantitative understanding of the electronic and ionic roles regarding charge-transfer phenomena poses a central challenge. Here, the electronic and ionic structure is simultaneously investigated at the prototypical charge-transfer heterointerface, $LaAlO_3/SrTiO_3$. Applying in situ photoemission spectroscopy under oxygen ambient, ionic and electronic charge transfer is deconvoluted in response to the oxygen atmosphere at elevated temperatures. In this way, both the rich and variable chemistry of complex oxides and the associated electronic properties are equally embraced. The interfacial electron gas is depleted through an ionic rearrangement in the strontium cation sublattice when oxygen is applied, resulting in an inverse and reversible balance between cation vacancies and electrons, while the mobility of ionic species is found to be considerably enhanced as compared to the bulk. Triggered by these ionic phenomena, the electronic transport and magnetic signature of the heterointerface are significantly altered.

Heterointerfaces of transition metal oxides exhibit astonishing and diverse properties including insulator-to-metal and nonmagnetic-to-ferromagnetic transitions. These intriguing characteristics hold great potential for the implementation of novel devices with combined functionality for electronics applications.[1,2] Phase-pure transition metal oxides exhibit a variety of fascinating phenomena as their electrical properties are highly sensitive to defect structure and lattice disorder.[3–7] However, when two of these materials are combined at the nanoscale, new electronic phenomena can arise. The abrupt interface constitutes a break of symmetry in chemical, as well as electronic environment, resulting in a strong coupling between orbital, spin, lattice, and ionic degrees of freedom that dictates the electronic properties.[8] The downscaling from bulk materials[4,5] toward nanoscale thin films[9–11] and functional interfaces[12–14] has opened new opportunities to functionalize oxides, but has also led to new

M.-A. Rose, Dr. F. Gunkel
Institute for Electronic Materials (IWE 2), and Juelich-Aachen Research Alliance for Fundamentals on Future Information Technology (JARA-FIT)
RWTH Aachen University
52074 Aachen, Germany
E-mail: rose@iwe.rwth-aachen.de

M.-A. Rose, Dr. M. Andrä, Prof. R. Dittmann, Dr. D. N. Mueller, Dr. F. Gunkel
Peter Grünberg Institute 7
Forschungszentrum Jülich GmbH, and JARA-FIT
52425 Jülich, Germany
E-mail: dav.mueller@fz-juelich.de; f.gunkel@fz-juelich.de

Dr. B. Šmíd, Dr. M. Vorokhta
Department of Surface and Plasma Science
Faculty of Mathematics and Physics
Charles University
Prague 180 00, Czech Republic

The ORCID identification number(s) for the author(s) of this article can be found under https://doi.org/10.1002/adma.202004132.

DOI: 10.1002/adma.202004132

Dr. I. Slipukhina, Prof. M. Ležaić
Peter Grünberg Institute 1 and Institute for Advanced Simulation
Forschungszentrum Jülich GmbH and JARA-FIT
52425 Jülich, Germany

Dr. H. Bluhm
Chemical Sciences Division
Lawrence Berkeley National Lab.
Berkeley, CA 94720, USA

Dr. H. Bluhm
Department of Inorganic Chemistry
Fritz Haber Institute of the Max Planck Society
14195 Berlin, Germany

Dr. T. Duchoň, Dr. D. N. Mueller
Peter Grünberg Institute 6, and JARA-FIT
Forschungszentrum Jülich GmbH
52425 Jülich, Germany

Prof. S. A. Chambers
Physical and Computational Sciences Directorate
Pacific Northwest National Laboratory
Richland, WA 99354, USA

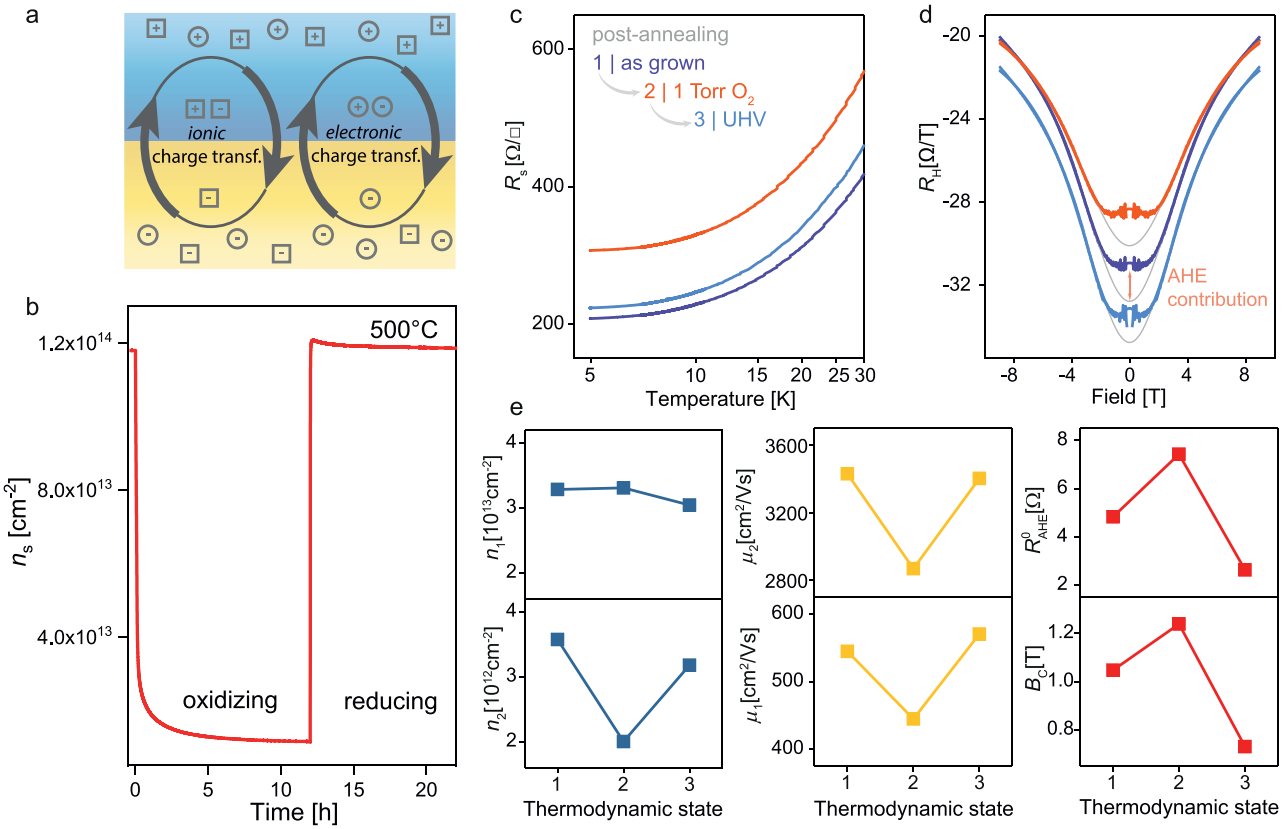

Figure 1. a) Schematic illustration of ionic and electronic charge transfer across oxide heterointerfaces. b) Sheet carrier density of 8 uc LAO/STO over time under different oxygen partial pressures. c) Low-temperature resistivity from a sample of 4 uc LAO/STO, quenched from similar annealing conditions. d) Hall coefficient measured at 5 K, whereas the gray lines indicate a two-channel fitting of the nonlinear Hall effect. The remaining discrepancy can be associated with the anomalous Hall effect. e) Hall data analysis resulting from a two-channel fitting including the anomalous Hall effect contribution (corresponding fits are displayed as solid lines in (d)).

challenges in understanding ionic–electronic phenomena in low-dimensional systems. The highly complex interplay of local defect structure and strongly confined electronic structure can induce multiple electronic and ionic phenomena at oxide interfaces.[1,2,15–20] One prime example of such an interface is the $LaAlO_3/SrTiO_3$ (LAO/STO) heterointerface where the polar nature of LAO induces charge transfer into the neighboring STO, generating a 2D-electron-gas (2DEG) at the interface of the two nominally insulating compounds.[15,21–23] Free electrons are generated without local dopants. As a result, enhanced mobility[24,25] is observed and quantization effects, field-tunable superconductivity as well as coexisting ferromagnetism and superconductivity become accessible in this nanoscale charge-transfer oxide system.[21,26–30]

However, charge transfer at oxide heterostructures consists of electronic and ionic contributions (**Figure 1**a). The ionic structure of oxide heterostructures is typically controlled kinetically during synthesis[28,31–33] or thermodynamically during post-synthesis thermal treatments.[34–36] The latter triggers ion dynamics tending toward thermodynamic equilibrium, and in principle heals growth-induced defects such as excess oxygen vacancies.[34] In STO, the resulting defect equilibria are highly sensitive to the applied thermodynamic conditions, implying that the chemistry and ionic structure respond to changes in ambient conditions.[4] This leads to the creation of oxygen vacancies in reducing conditions and Sr vacancies in oxidizing conditions.[4,37,38] Sr vacancies are commonly disregarded since in undoped crystals, they have a lower concentration,[39,40] a higher formation energy, and a lower diffusion coefficient than oxygen vacancies[41] (for comparison, at 500 °C the respective vacancy diffusion coefficients are $D_{V_{Sr}''} = 3\times10^{-23}$ cm^2 s^{-1} [5] and $D_{V_O^{\cdot\cdot}} = 1\times10^{-7}$ cm^2 s^{-1} [42]). However, the presence of electrons (as induced, e.g., via donor-doping) can drive strongly enhanced effects of Schottky disorder.[3–5,43] At surfaces of n-doped STO, Sr vacancies were found to be rather mobile while their generation leads to a depletion of free carriers and upwards band bending toward the surface.[5,44] This implies that for confined systems the role of ionic species, traditionally regarded as "slow" with respect to other processes, can be much more important than for bulk crystals.

In oxide heterostructures, the buried interface generates additional complexity in characterizing ionic and electronic charge-transfer contributions, posing a considerable experimental challenge: A detailed depth profiling of electronic structure and interface chemistry via energy-tunable synchrotron radiation is indispensable. Moreover, an in situ approach is

required to comply with the ionic response times to a varied atmosphere, which can be rather fast even at relatively low temperatures.[45]

Herein, we show that the electric and magnetic properties of the LAO/STO interface can be reversibly changed via control over the ionic charge transfer at the interface. The ionic contribution is controlled by annealing at typical post-deposition conditions (470 °C, 0.001–1 Torr O_2). By using in situ X-ray photoelectron spectroscopy (XPS) under applied thermodynamic conditions (near-ambient pressure (NAP)-XPS), we identify the ionic species contributing to the ionic–electronic charge transfer and show how the interface chemistry evolves while the thermodynamic conditions are varied. Based on spectroscopic depth profiling, the complex chemistry and nature of ionic charge transfer are deconvoluted: Diffusion of Sr ions toward the LAO surface and precipitation of secondary Sr-phases on the surface triggered by the oxygen environment leads to a depletion of the 2DEG and the formation of Sr vacancies. Motion of Sr ions across the interface reflects an ionic charge-transfer process that accompanies 2DEG formation and directly couples to electron mobility and magnetic behavior obtained at the interface. This showcases how ionic defect equilibria influence the electronic charge transfer in confined oxide systems already at temperatures much lower than observed in the bulk and how the balance of electronic and ionic species is jointly responsible for the rich physics of oxide heterostructures.

The inherent tunability of electronic and magnetic properties of the LAO/STO heterointerface is demonstrated by a combination of high temperature treatments and low temperature characterization. In electrical conductivity relaxation (ECR) experiments, LAO/STO heterostructures were exposed to varying gas compositions in order to achieve different oxygen activities, while measuring their interface conductivity. All samples were fabricated by pulsed laser deposition (PLD) and characterized via atomic force microscopy and Hall measurements beforehand to ensure high-quality thin films (see Section S1, Supporting Information). As shown in Figure 1b, a distinct and reversible electrical response of the 2DEG to changes in oxygen atmosphere was detected at a temperature of 500 °C (note that this corresponds to a typical temperature applied to oxide heterostructures during and after growth).[33] Because of the elevated temperature, we can explore the equilibration behavior of the interface under different thermodynamic conditions by monitoring the actual electron density over time. Electronic relaxation typically takes place on picosecond time scales, so that relaxation behavior on longer time scales is ascribed to ionic relaxation. When oxidizing conditions (pO_2 = 1 Torr) are applied, a rapid decrease in sheet carrier density (n_s) is observed, approaching a value roughly one magnitude lower than in the pristine state. As reducing conditions ($pO_2 \approx 1 \times 10^{-19}$ Torr, 4% H_2/Ar atmosphere, note that the given pO_2 value refers to the chemical oxygen partial pressure achieved in this gas mixture) are applied, the reverse process is observed as n_s recovers its original value. This value of roughly 1×10^{14} cm^{-2} achieved in reducing environment, corresponds well to the Hall data measured in the as-grown sample and is typical for the 2DEG of LAO/STO.[20,34,46,47] Reference measurements on bare STO showed significantly lower conductivity under similar conditions, excluding a contribution from the underlying STO substrate to the conductivity measurements (see Section S2, Supporting Information). The fully reversible electrical response shows that a reversible ionic process is responsible for the changed electronic properties of the interface.

To further investigate the impact of ionic constitution on the two distinct states observed in the ECR experiments, samples were quenched in different atmospheres and their low-temperature transport behaviors were characterized. In Figure 1c, we compare the as-grown state to different post-annealed states obtained from the same sample (4 uc/1.5 nm LAO on STO). The sample was first annealed in a furnace (oxidation at pO_2 = 1 Torr, 470 °C) that allows rapid quenching to room temperature by quickly moving the sample from the hot to the cold region of the furnace. This process effectively freezes the ionic state established at elevated temperatures within seconds (≤10 s).[48] After the measurement, the same sample was annealed under UHV conditions (reduction at 1×10^{-8} Torr base pressure, 470 °C) and then quenched again, thereby imitating the oxidized and reduced states applied in the ECR experiment (Figure 1b). The low-temperature characterization demonstrates a change in resistivity induced by the annealing process in oxidizing conditions that fully recovers after subsequent annealing in UHV, again emphasizing the reversibility of the thermodynamic process (Figure 1c). Additional low-temperature Hall measurements give insight into electron scattering processes (low-temperature mobility) and reveal potential signatures of magnetism (anomalous Hall effect) at the interface.[24,49–51] A two-carrier fitting model consisting of high-density–low-mobility (n_1, μ_1) and low-density–high-mobility (n_2, μ_2) electrons, including an anomalous Hall contribution, was applied to the Hall coefficient (R_H) as seen in Figure 1d. Further details on the evaluation of the nonlinear Hall effect and anomalous Hall component are presented in Section S3, Supporting Information. The resulting fitting parameters are depicted in Figure 1e. Both carrier density (n_2) and mobility (μ_1, μ_2) dropped when the sample was exposed to the oxidizing anneal. Moreover, both parameters recover when the sample was subsequently annealed in UHV. Hence, the 2DEG at the LAO/STO interface is depleted through annealing in oxidizing conditions, indicating a variable (and reversible) contribution from electronic charge transfer at the interface. At the same time, the mobility change indicates that additional defects are incorporated at the interface when exposed to oxygen-rich atmosphere. An alternative explanation for the lowered mobility would be an orbital reconstruction through the changed carrier density. This was discussed for example by Doennig et al.[52] where it was suggested that a change in local carrier density may lead to a population of different bands in the Ti 3*d*-orbital, changing the effective mass of electrons occupying the 2DEG.

Remarkably, the oxidized sample also shows an enhanced anomalous Hall component, characterized by the critical field B_c and the amplitude R^0_{AHE} (Figure 1e) after oxygen-rich treatment that also varies in a reversible manner after the subsequent reducing treatment. The anomalous Hall contribution is related to the presence of magnetic moments in the system that leads to a spin polarization of charge carriers, which could be seen in multiple studies where a direct scaling of magnetism to the anomalous Hall coefficient could be seen.[53–55] Also, in the context of oxide heterostructures, the AHE is used to identify

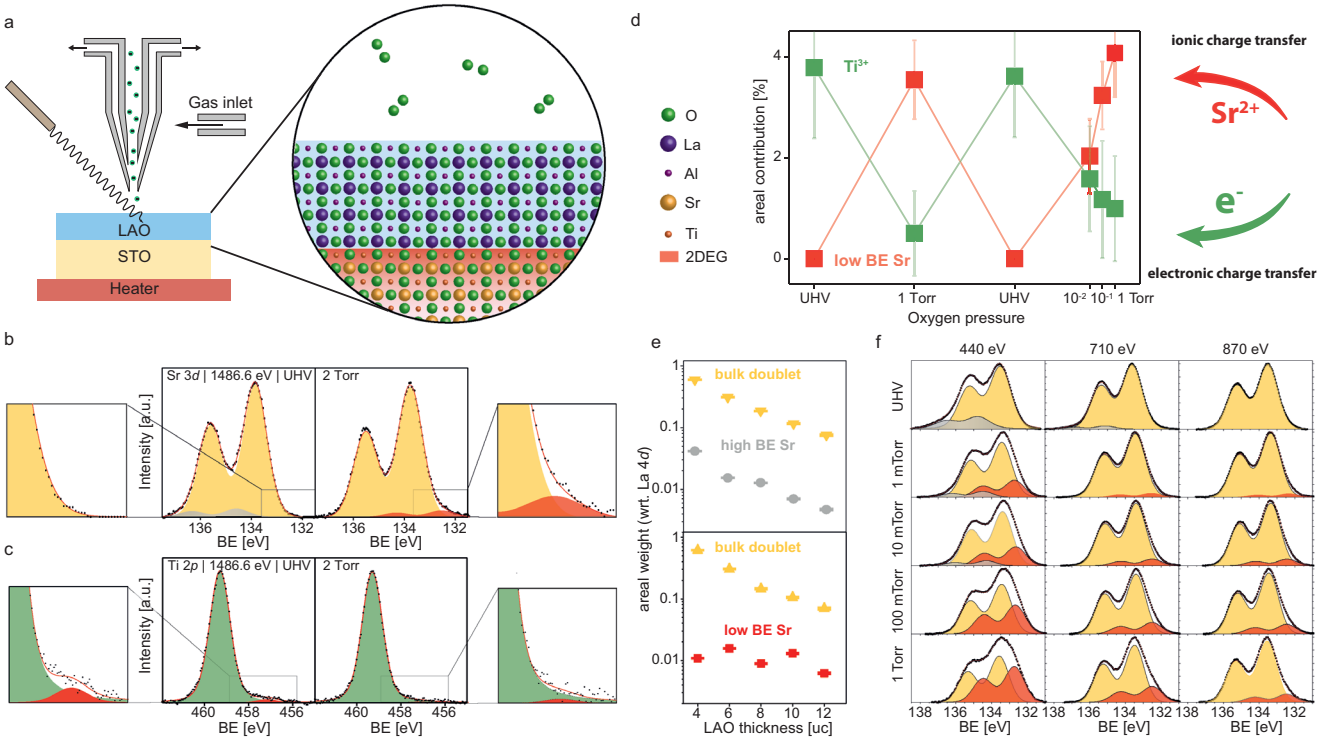

Figure 2. a) Sketch of the NAP-XPS setup and sample geometry. b) Experimental data and fitting of the Sr 3*d* spectra for a sample of 6 uc LAO on STO. c) Fitting of the Ti 2*p* core-level spectra from the same sample. d) Area ratios of the obtained fits over the applied pressure steps. e) Sr 3*d* doublet intensities normalized to the La 4*d* spectra over increasing sample thicknesses. f) Fitting of the Sr 3*d* core-level spectra of a 4 uc LAO/STO sample under synchrotron radiation.

magnetism in transport properties.[49–51,56] These results are consistent with the behavior of LAO/STO samples in thermodynamic equilibrium commonly observed at higher annealing temperatures.[50,57] Based on low-temperature transport analysis, an altered state of the interface characterized by lower mobility, enhanced magnetic signature, and a depleted 2DEG (lower carrier density) are obtained in the oxidized condition.

The key question arising from these results is how the sample changes structurally and chemically in these different environments: Sample-to-sample variations can be excluded as these data were recorded for the same sample and only different post-annealing procedures were applied. Furthermore, the effect of removing growth-induced excess oxygen vacancies during annealing can be excluded due to the observed reversibility (excess oxygen vacancies would not have any driving force to recover after being removed).[33–35,58] In order to investigate this phenomenon in more detail, we employ NAP-XPS which enables probing interface chemistry in presence of gases while the thermal processing is carried out.

The chemical and electronic reconstruction of the interface under the applied atmospheres was investigated using NAP-XPS (**Figure 2**a) with which we probed the chemical and electronic states of the buried heterointerface directly while supplying oxygen and heat in situ (T = 470 °C, $pO_2 \leq 4$ Torr). Major changes in peak shapes were detected in the Sr 3*d* and Ti 2*p* core-level spectra (Figure 2b,c), while the Al 2*p* and La 4*d* spectra did not change in any significant way as the oxygen pressure was varied (Section S4, Supporting Information). The O 1*s* spectra showed a slight broadening while exposed to oxygen as shown in detail in Section S4, Supporting Information. All spectra showed shifts to lower binding energies (BEs) by different amounts which will be discussed in detail below. Most interestingly, however, NAP-XPS reveals correlated changes in the Sr 3*d* and the Ti 2*p* core-level spectra as the oxygen atmosphere was varied (Figure 2b,c). These correlated changes include the concomitant appearance of an additional Sr feature at lower BE (low-BE-Sr, red area in Figure 2b) and disappearance of a substantial Ti 2*p* contribution from Ti^{3+} ions (red area in Figure 2c), also at lower BE,[59] when the heterostructure is exposed to oxygen. It is observed that the Ti^{3+} contribution is strong in more reducing conditions (UHV), while the low-BE-Sr component is weak. In contrast, under applied oxygen, the Ti^{3+} component is weak and the low-BE-Sr component becomes much more intense. Moreover, the appearance of the low-BE-Sr is reversibly correlated to the depletion of carriers from the 2DEG, as detected by the weakening of the Ti^{3+} feature (Figure 2d). This correlation is observed in all samples and shows little or no sign of degradation for all three oxidation–reduction cycles that were measured in our experiment (Figure 2d). This result suggests a coupling of the electronic response of the interface (via Ti^{3+}) and the associated chemical response (via low-BE-Sr).

In order to elucidate the chemical structure of the interface, synchrotron-based NAP-XPS was employed for which the information depth increases with increasing incident photon energy (PE). The results for the Sr 3*d* core-level spectra are displayed in Figure 2f. More surface-sensitive measurements are made at lower PE (440 eV) and more bulk-sensitive measurements at

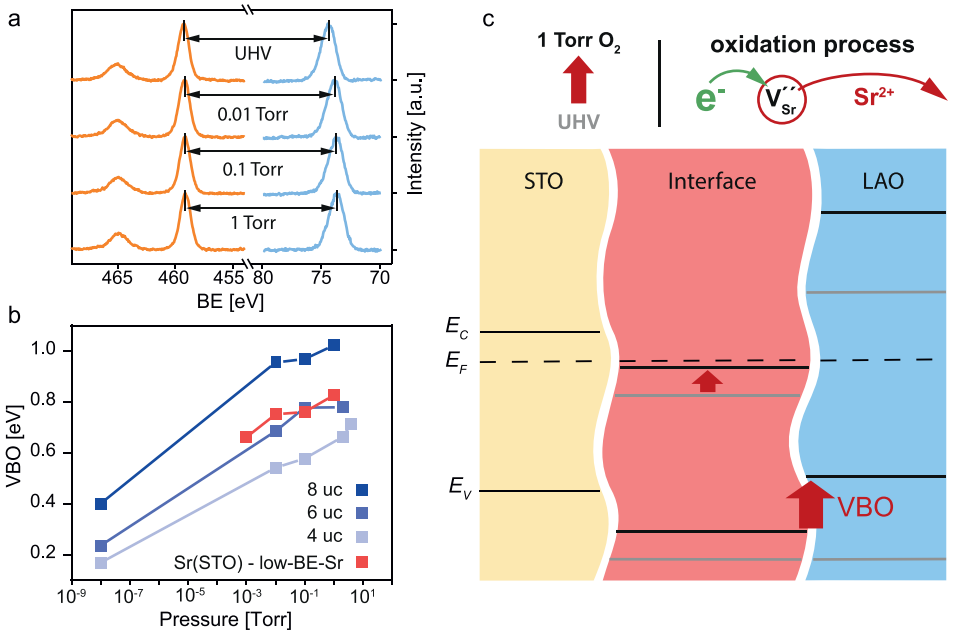

Figure 3. a) Background corrected Ti 2p and Al 2p spectra of 6 uc LAO on STO. b) VBO over oxygen partial pressure, calculated from binding energy shifts determined in (a) for varying LAO thicknesses. c) Band structure sketches interpreting the shifts seen in (b).

higher PE (870 eV) (left to right in Figure 2f). Again, elevated temperature (470 °C) and different oxygen partial pressures ranging from UHV to 1 Torr of oxygen were used, reflecting reducing and increasingly oxidizing conditions (top to bottom in Figure 2f). Three doublets are necessary to accurately reproduce the Sr 3*d* line shape at different probing depths and oxygen partial pressures. In the oxygen-poor environment, the Sr 3*d* spectrum exhibits the classical shape consisting of two doublets reflecting Sr in the STO crystal lattice and a surface/interface component at higher BE (grey area in Figure 2f). The high-BE component is interpreted as Sr in a chemical environment that differs from that in bulk STO, meaning a changed Madelung potential[60,61] which in this case may be caused by the proximity of the neighboring oxide layer and the altered potential experienced by Sr ions inside of the interfacial well. In the oxygen-rich environment, however, the lower BE feature (red area Figure 2f) appears and makes a significant areal contribution to the total spectrum in most surface-sensitive measurements (bottom-left in Figure 2f). Significantly, the intensity of the low-BE-Sr component scales with the oxygen partial pressure, thereby corroborating that this secondary Sr species is formed through the oxidation process (pO_2-dependence) and accumulates in proximity of the heterostructure's surface (PE-dependence). At the same time, the intensity of the secondary component at higher BE is diminished when oxygen is reintroduced.

In order to determine the depth distributions of these three species within the heterostructure in more detail, different LAO thicknesses were investigated and the spectral intensity scaling with overlayer thickness was analyzed (cf. ref. [62]). In this case, an interfacial phase is expected to be attenuated exponentially with LAO film thickness, whereas a surface phase is expected to show similar intensity, independent of overlayer thickness. As we find, the bulk component and the high-BE-Sr component (observed in reducing conditions) show exponential attenuation with LAO film thickness, whereas the low-BE-Sr component (observed in oxidizing conditions) does not scale significantly with LAO thickness, indicating that this component is located close to or at the surface (Figure 2e). A more detailed analysis can be found in Section S5, Supporting Information. Therefore, the low-BE-Sr component shows the characteristics of a Sr species that is displaced from the interface, indicating diffusion of Sr ions through the LAO thin film and eventual precipitation on the surface of the heterostructure. The Sr vacancies left behind at the interface trap itinerant electrons from the 2DEG upon formation, which is consistent with the diminished Ti^{3+} signature observed in the Ti 2*p* spectra.[63] The spectral data reveal that this process is fully reversible, indicating that Sr moves from the interface to the surface and back again as the oxygen gas activity is cycled.

The apparent diffusion of Sr ions from the interface results in the low-BE-Sr species having a different local structural environment than in STO and this result holds the key to understanding the unusual BE of this feature.[64] A similar Sr 3*d* shift to lower BE was also reported for STO overlayers on LAO/STO heterostructures[65] and for lanthanum strontium ferrite thin films on STO.[64] These shifts are influenced by band alignment across the heterostructure as effective band shifts affect the energies of all core-levels. In order to disentangle chemical from electronic BE shifts, a detailed assessment of the band alignment at the interface is required.

The electronic structure of the heterojunction in the different thermodynamic environments can be determined from the apparent BEs as the ambient pO_2 is varied. In accordance with the literature, we assume a close to flat band scenario within the LAO layer under UHV conditions, which is motivated by the absence of significant core-level broadening.[66–69] In **Figure 3**a,

we show Al 2*p* and Ti 2*p* spectra as a function of oxygen partial pressure for 6 uc LAO/STO. In the absence of interfacial chemistry, BE shifts reflect changes in the electrostatic potential of the LAO and STO, respectively. The Ti 2*p* spectrum shifts about 0.1 eV to lower BE as oxygen is introduced. In contrast, the Al 2*p* spectrum shifts by about 0.6 eV to lower BE. Moreover, the Al 2*p* peak shift in oxygen ambient increases to ≈1 eV with increasing LAO overlayer thickness (see Section S6, Supporting Information) whereas the Ti 2*p* shift remains small and is independent of LAO overlayer thickness. The same behavior is observed when using the Sr 3*d* and La 4*d* spectra to monitor the STO and LAO, respectively (cf. Section S6, Supporting Information). A shift in the apparent BE to lower values for any of these core-levels reflects movement of the Fermi level deeper into the bandgap,[44,45] and is consistent with a depletion of the 2DEG when oxygen is applied. The general trend observed, is thus consistent with the disappearance of the significant Ti^{3+} contribution under oxidizing conditions (Figure 2c). However, the monotonic change in energy difference between film and substrate core-levels with oxygen partial pressure, indicated by the arrows in Figure 3a, signals a change in the band alignment.

Two possible scenarios may be considered to explain this behavior: i) the development of an electric field in the LAO layer, and, ii) a changing valence band offset (VBO) at the interface. In the first case, a broadening of the Al 2*p* and La 4*d* features is expected, provided the magnitude of the built-in potential is not much smaller than the characteristic peak width.[68] However, no peak broadening is observed (see Section S4, Supporting Information) and this result establishes an upper limit for the built-in potential in the LAO. In the second case, the VBO can be determined from the energy differences between the substrate and film peaks[68] (see Section S7, Supporting Information). The resulting VBOs obtained for different LAO overlayer thicknesses and different oxygen atmospheres are shown in Figure 3b. In the literature, the VBO between LAO and STO is typically found to be close to zero and is attributed to the similar O 2*p* character of the valence band in both oxides.[68,70] A VBO close to zero is also determined from our spectra measured in UHV. In oxygen atmosphere, however, an increase in VBO of ≈0.6 eV is measured, and the VBO rises to 0.9 eV with increasing LAO thickness.

As seen in Figure 3b, the energy difference between the bulk component and the low-BE component observed in the Sr 3*d* core-level spectra (shown as red data points) correlates with the VBO as expected, if the low-BE feature is due to Sr atoms in lattice sites on or near the LAO surface. This indicates that Sr ions occupy lattice sites with a Madelung potential comparable to that at A-lattice sites in the perovskite structure, namely, La vacancy sites in the LAO layer or surface sites with comparable coordination.[64,65,68]

The thickness dependence of the observed BE differences (Ti 2*p* – Al 2*p* and Sr 3*d* – La 4*d*) is probably not solely due to changes in VBO as there is no obvious reason why the VBO should depend on the LAO thickness. In contrast, this result may be due to the development of a small, uncompensated field across the LAO layer as oxygen atmosphere is applied. We note that simulations of the Al 2*p* line shape show that a built-in potential of 0.1 eV nm^{-1} can induce the observed BE shifts without measurably broadening the spectrum (see Section S8, Supporting Information). Considering that a field across the LAO layer could change from tilting downwards to upwards, this yields a lower detection limit of a 0.2 eV nm^{-1} gradient. A complete attribution of the observed shifts to a linear potential, however, would result in an even higher slope of 0.3–0.4 eV nm^{-1}, which should be detectable through significant peak broadening.

This uncompensated field could be due to the partial filling of LAO surface oxygen vacancies (which have been suggested as the driver behind electronic reconstruction)[71] when exposed to oxygen atmosphere.[66]

The BE of the low-BE-Sr component is at a highly unusual value, as throughout the current literature secondary components in STO based systems are almost exclusively reported at the higher BE side with respect to bulk STO.[44,60,61] Exotic defect states, such as complex Sr/Ti anti-site defects were reported to yield low BEs,[72] but these are unlikely to form in a reversible manner under the light thermodynamic treatments in our study. Therefore, we assign the observed low-BE component to be a result of the band structure of the LAO/STO heterostructure and particularly to Sr components located in or on the LAO layer. A similar phenomenon to occur during growth was found by Treske et al.[62] The dynamic and reversible change in the Sr core-level with pO_2, however, indicates that the precipitation/out-diffusion of Sr ions is not fixed after growth, but actively contributes to thermodynamic equilibration of the interface.

It is evident from our low-temperature conductivity measurements that annealing in oxidizing conditions leads to a depletion of the 2DEG, a lowered electron mobility, and an enhanced magnetic signature in the 2DEG. These aspects can be directly linked to our chemical analysis by NAP-XPS, in which the depletion of free carriers is detected and correlated to the diffusion of Sr ions to the surface and subsequent precipitation as secondary phase in oxidizing environment. While the lowered carrier density and mobility can be intuitively linked to the incorporation of Sr vacancies, the origin of the magnetic signature could also be only indirectly related to the cation migration due to effects like local strain, or stronger localization caused by the lowered mobility.

Previous studies have suggested that the Schottky equilibrium of the Sr cation lattice could explain some of the behavior observed at elevated temperature.[11,73] The complex nature of the heterointerfaces, however, may implicate other defect-scenarios with contributions from both STO and LAO defect sites. Given the reported importance of oxygen vacancies for the properties of LAO/STO interfaces,[35,74,75] it needs to be considered if annihilation and incorporation of oxygen vacancies alone can explain all observed data consistently. For one, however, the reversibility of the appearance of the Ti^{3+} signature in the Ti 3*d* core-level rules out a mere effect of growth-induced excess oxygen vacancies on the STO side of the interface. Second, the concentration of oxygen vacancies in the bulk of the LAO thin film compensating for the cation nonstoichiometry of the thin film[3] is widely fixed and cannot explain the varying electron concentration alone. Finally, oxygen vacancies formed at the surface of LAO to compensate charge on the LAO side of the interface[66,71] may vary in different oxygen ambient and therefore influence the density of itinerant electrons at the interface. However, none of these scenarios can explain the

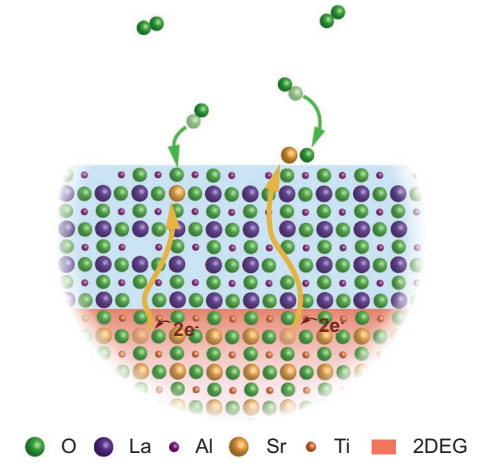

Eq. 1 $$Sr_{Sr}^{x} + \frac{1}{2}O_2\,(g) + 2e' \rightleftarrows V_{Sr}^{''} + SrO_{s.p.}$$

Eq. 2 $$[Sr_{Sr}^{x} + \frac{1}{2}O_2\,(g) + 2e']_{STO} + [V_{La}^{'''} + \frac{3}{2}V_{O}^{\cdot\cdot}]_{LAO} \rightleftarrows [V_{Sr}^{''}]_{STO} + [Sr_{La}^{'} + O_{O}^{x} + \frac{1}{2}V_{O}^{\cdot\cdot}]_{LAO}$$

Figure 4. Illustration of possible Sr configurations and the resulting partial Schottky equilibria considering surface precipitation of SrO (right-hand process in sketch, Equation 1) or the involvement of LAO defect sites (left-hand process in sketch, Equation 2).

distinct and reversible behavior of the Sr 3*d* core-level spectra. This strongly indicates that while oxygen vacancies may play a crucial role in providing "positive" charge on the LAO side of the interface, Sr ions (vacancies) are involved to partially provide the negative counter-charge on the STO side of the interface. The dynamic response of the Sr 3*d* core-level to a varied oxygen pressure implies the sufficient mobility of Sr ions under experimental conditions.

Figure 4 illustrates two scenarios, describing the release of Sr ions from the STO lattice upon exposure to oxygen. The formation of Sr vacancy defects upon interaction with ambient oxygen (O_2(g)) and the consumption of electrons are described in Equation 1 in Figure 4. As a result, the removed Sr cations (Sr_{Sr}^{x}) typically form SrO surface precipitates ($SrO_{s.p.}$). The primary driving force for this process is the uptake of oxygen from the ambient, controlled by the surrounding oxygen partial pressure and concentration of available electrons. Since a highly dense electron gas is present directly at the interface in the LAO/STO system, a large driving force for the Schottky equilibrium to form Sr vacancy defects is present. This diffusion of Sr ions from the interface through the heterostructure involves an additional intermediate reaction step involving LAO defect sites: Sr diffusion must take place via La vacancies within the LAO layer, which are naturally formed during synthesis of the thin films,[76–78] and even support 2DEG formation.[77] At the same time, the LAO thin film contains a finite reservoir of oxygen vacancies, first, to compensate cation-nonstoichiometry[11,77,79] and, second, to compensate the interface dipole at the surface of the LAO thin film.[71] The diffusion of Sr ions from the interface and concomitant uptake of oxygen by filling oxygen vacancies in the LAO layer is facilitated through the presence of both La vacancies and oxygen vacancies in the LAO overlayer. Note that consistent with literature[77,79] a stoichiometry evaluation based on XPS data revealed a slightly La-poor composition of our thin films, which generally permits La vacancies to form. The resulting defect reaction can be expressed as shown in Equation 2 in Figure 4. The incorporation of Sr on a La vacancy site and the uptake of oxygen results in an unchanged net polarization in the LAO layer, leaving the general charge-transfer process unaffected.[71,77,79] Upon diffusion of Sr ions toward the surface via La vacancy sites, this process eventually transforms into Equation 1, once Sr starts to agglomerate at the surface of the LAO layer. Both equations describe the thermodynamic equilibrium state in a given oxygen partial pressure leading to a higher concentration of Sr vacancies in higher pO_2, as the chemical reaction is driven more to the right-hand side. The reverse process, a lowered Sr vacancy concentration and reincorporation of Sr in more reducing conditions can be understood in the same manner, where the reaction is driven more to the left-hand side of the equations.

In order to corroborate that this microscopic picture is energetically favored, we performed density functional theory (DFT) calculations for the atomic configurations, shown in **Figures 5**a–e, including their respective total energy (the lowest energy is set to zero). We first compare the ideal heterostructure including an O_2 molecule in vicinity of the surface (Figure 5a) with two resulting configurations due to the oxygen exposure. These include an adsorbed oxygen atom at the surface (Figure 5b) and a defective heterostructure in which a Sr ion is moved from the interface to the surface and is bound to one oxygen atom (Figure 5c). This configuration mimics the process described by Equation 1 in Figure 4. Second, we compare a heterostructure with a La–O Schottky defect in the overlayer, also in the presence of an O_2 molecule near the surface (Figure 5d), to the interface configuration with a Sr moved into a La vacancy site with the oxygen vacancy filled (Figure 5e). This imitates the process described by Equation 2 in Figure 4. The resulting total energies clearly indicate that the formation of a Sr vacancy defect at the interface and subsequent precipitation into the LAO overlayer and at the surface is energetically favorable for the LAO/STO heterostructure upon oxidization. Both processes result in an exothermic reaction bringing the total energy of the system to a minimum and therefore support the proposed interpretation.

To analyze the effect of Sr precipitation to the LAO surface on the electronic properties of LAO/STO, we calculated the spin-polarized electronic density of states (DOS), shown in Figure 5f,g. For the ideal LAO/STO heterostructure one can observe a shift of the LAO band edge deeper into the bandgap (potential build-up). This results in an overlap of the LAO surface states and the interfacial TiO_2 conduction band states, enabling the electronic charge transfer (Figure 5f) and conductivity due to the partially filled Ti 3*d* states. The electronic DOS changes drastically, when Sr precipitation as shown in Figure 5c is introduced (Figure 5g). While eliminating the electronic potential build-up and reducing the overlap between LAO valence and STO conduction states, a diminished occupation of Ti 3*d* states at the interface is observed. This result stands in agreement with the 2DEG depletion upon oxidization as could be observed through

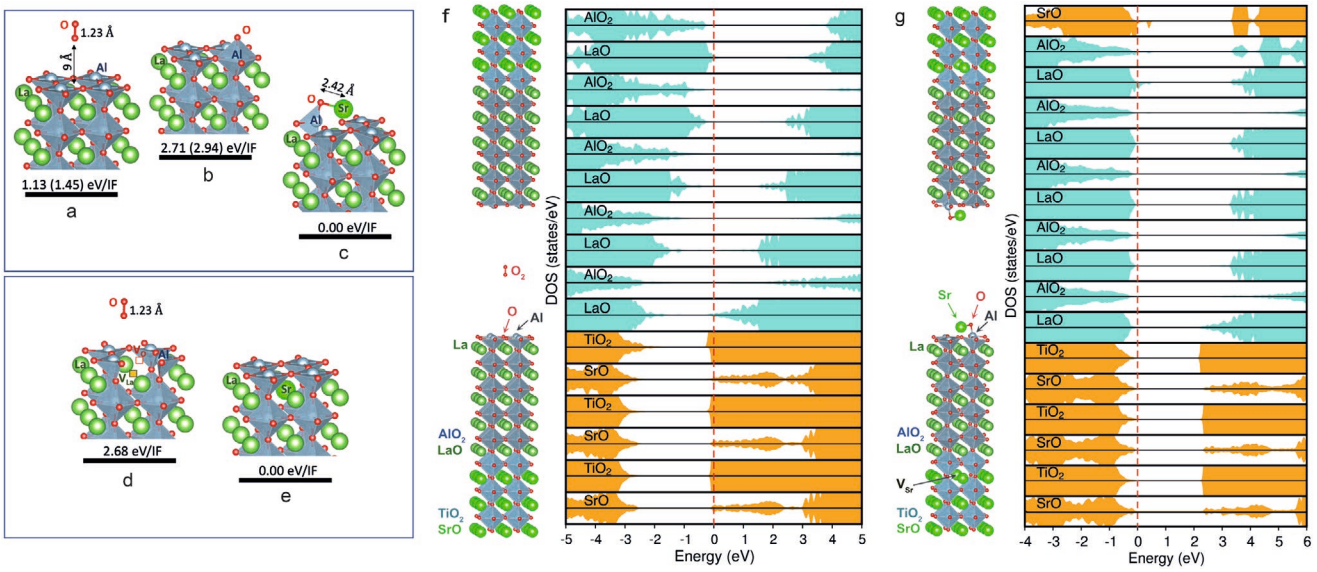

Figure 5. a–e) Relative energetic stability of LAO/STO slab under oxidizing conditions obtained from DFT: ideal interface with an oxygen molecule nearby (a); ideal interface with the atomic oxygen, adsorbed on an AlO_2-terminated surface atop the Al site (b); interface with a single Sr vacancy and SrO precipitate on an AlO_2-terminated surface (c); ideal interface with La and O vacancies in the LaO overlayer upon oxidizing conditions (d); the interface with a Sr moved from the interface to a La vacancy site together with oxygen occupying the O vacancy site in the LaO overlayer (e). The values are obtained at $U_{Ti} = 4$ eV. The numbers in parentheses were obtained at $U_{Ti} = 7.4$ eV for comparison (cf. Experimental Section). Note: For simplicity only the surface and the upper layers of the simulation slab are shown. f,g) Structural model and the layer-resolved spin-polarized DOS for LAO/STO slab under oxidizing conditions (obtained at $U_{Ti} = 4$ eV). Ideal interface with an oxygen molecule nearby (similar to (a)) (f); the interface with a single Sr vacancy and SrO precipitate on an AlO_2-terminated surface (similar to (c)) (g). The red dashed line represents the Fermi level position. The upper (lower) part of each graph corresponds to spin-up (spin-down) DOS, correspondingly.

the diminished Ti^{3+} ions (Figure 2c) and supports that the potential build-up can be ionically compensated through an active Schottky equilibrium (Equations 1 and 2 in Figure 4).

Our results hence show that Sr ions can be much more active at the spatially confined interfacial region of oxide heterostructures compared to bulk crystals. The macroscopic diffusion coefficient in bulk STO renders Sr vacancies effectively immobile at temperatures well below 1000 °C. However, in LAO/STO the mobility of Sr ions and vacancies is remarkably enhanced, even allowing the migration of ionic species into and through the LAO overlayer, showcasing unusually high mobility of cations. This result may apply to surfaces[44,45,80] and complex oxide interfaces in general. In the case of LAO/STO, it is resolving the polar catastrophe via ionic charge transfer that drives the system into a fully reversible, more defective state with enhanced lattice disorder in the cation sublattice (when exposed to oxygen). This phenomenon arises from the fact that in complex oxides both electronic and ionic species can contribute to charge-transfer processes.

Our investigation reveals that a purely electronic paradigm to understand the nature of charge transfer at oxide heterostructures is insufficient to fully explain the observed emergent phenomena: Ionic charge-transfer plays a crucial role for these systems, having direct impact on electrical and magnetic properties. Ionic–electronic charge transfer is much more effective in driving functional properties at oxide heterostructures than might be expected based on bulk behavior, and results in a complex correlation between electronic/magnetic phenomena and details of ionic structure. As demonstrated, confinement and lower dimensionality, broken symmetry, large local electric fields, and the presence of defects have the potential to enhance and trigger ionic processes not accessible at similar temperatures in bulk materials. The mobility of ionic species is strongly enhanced in defective heterostructures, allowing Sr cations to penetrate through the LAO overlayer to the surface, driven by the altered energetics and defect dynamics at the confined interface. The associated ionic charge transfer has direct impact on the electronic properties of the interface and is accompanied by emergent magnetism, underscoring the strong coupling of electronic and ionic structure in oxide heterointerfaces. Carefully conceived thermodynamic treatments can therefore tailor the properties of the interface to allow control of the carrier density and mobility and to trigger magnetic properties. NAP-XPS serves as a powerful tool to deconvolute the contributions of ionic motion and defect structure to the electrical properties. Our results show how both electric and ionic contributions must be considered when dealing with the chemical complexity of oxide heterostructures and their interfaces. Beyond emergent electronic phenomena, novel nano-ionic processes may also arise in nanoscale oxide structures, being derived from the enhanced mobility and driving forces for ionic motion. The high mobility of Sr ions observed in LAO/STO is illustrative of the rich physics and chemistry that occur in the transition from bulk to engineered nanoscale structures.

Experimental Section

Pulsed Laser Deposition: All samples were grown by PLD (Surface Systems and Technology GmbH & Co. KG, Germany) under similar

growth conditions on TiO_2-terminated STO (100) single crystals. A KrF excimer laser (λ_{laser} = 248 nm) was used with a repetition rate of 1 Hz on a single crystalline LAO target with a spot size of 2 mm^2 and a laser fluence of 0.96 J cm^{-2}. Target-to-substrate distance was set to 44 mm, under an oxygen partial pressure of 1×10^{-3} mbar. A backside laser heater was used to heat the substrates up to 800 °C. All samples were subsequently held in deposition conditions for 1 h to refill oxygen vacancies induced through the growth process.[34] The growth process was monitored using high pressure reflection high-energy electron diffraction. Clear intensity oscillations of the primary reflected spot were observed for all samples indicating a layer-by-layer growth mode. Representative data for a 8 uc thick LAO layer on STO can be found in Section S1, Supporting Information.

Hall Measurements: The samples were bonded using ultrasonic aluminum wire bonding. For low-temperature measurements, a PPMS (Quantum design) was used whereas samples were contacted by wire bonding in a mimicked Hall bar geometry.[50] The samples were cooled down to 5 K and magnetic fields from −9 to 9 T were applied. The magnetic field was also applied at temperatures of 6, 7, 8, 9, 10, 15, 30, 100, and 300 K. The recorded Hall data was anti-symmetrized and modeled by a two-electron-channel approach and an anomalous Hall effect contribution represented by $R_{AHE} = R^0_{AHE} \tanh(B/B_c)$ as described in ref. [50]. Further details on data analysis are given in Section S3, Supporting Information.

Near-Ambient Pressure X-ray Photoelectron Spectroscopy: NAP-XPS was carried out at Charles University, Prague, CZ using a lab-based system (SPECS Surface Nano Analysis GmbH, Al-$K\alpha$ source) and at Advanced Light Source (ALS), Beamline 11.0.2., Berkeley, USA for synchrotron-based experiments.[81] In both cases, NAP-XPS was similar to conventional XPS, but employs differential pumping in close proximity to the sample to allow sufficient photoelectron yield at increased gas pressure. To prevent charging effects two stripes of platinum were sputtered on all samples using a shadow mask and grounding contacts were applied. A set of samples with different LAO thicknesses (4, 6, 8, 10, and 12 uc LAO) was characterized to ensure comparable properties. These samples were then exposed to oxygen partial pressure, while being spectroscopically investigated. The La 4*d*, Al 2*p*, O 1*s*, Sr 3*d*, and Ti 2*p* core-level spectra and VB spectra were recorded. Prior to experiment, all samples were heated and exposed to oxygen to remove carbonates from the surface. During measurements the samples were kept at a constant temperature of 470 °C. This was the highest safely accessible temperature, which was chosen to be as close as possible to growth and annealing conditions. Experimental parameters at the ALS experiments were: pass energy = 20 eV, step size = 0.05 eV, and dwell time = 100 ms; and for Prague experiments: pass energy = 20 eV, step size = 0.05 eV, and dwell time = 200 ms.

Electrical Conductivity Relaxation: ECR experiments monitor the electronic response of the sample that was heated up to a defined temperature in a furnace where the atmosphere could be changed through inlet of different gas compositions. While the sample was reacting with its surrounding atmosphere the corresponding changes in conductance could be directly monitored using platinum wires and electrodes. The measured sheet resistivity was transferred into sheet carrier density (n_s) using the temperature depending electron mobility reported in ref. [82]. To achieve oxidizing conditions, mixtures of oxygen and argon gas were used. For the reducing conditions, a mixture of hydrogen and argon was applied to mimic UHV-like conditions. Samples were contacted via four-point geometry. The transition between different gas atmospheres was realized using a four-port valve to switch between two parallel flow channels, allowing rapid switching between gas flows. Therefore, the change of present gas atmosphere could be viewed as instantaneous with respect to the equilibration speed of the material under analysis.

Density Functional Theory: DFT calculations were performed with the Vienna Ab initio Software Package,[83–85] using the Perdew–Burke–Ernzerhof exchange-correlation functional[86] and the projector augmented wave pseudopotentials.[87] The energy cut-off and the Monkhorst–Pack k-points mesh were chosen to be 500 eV and $6 \times 6 \times 1$ ($9 \times 9 \times 1$ for DOS calculations), correspondingly. The electronic energy was converged to 10^{-5} eV, using Gaussian smearing with σ = 0.05 eV, and the atomic positions were relaxed until the forces on atoms were not larger than 5×10^{-2} eV $Å^{-1}$. As a structural model for the LAO/STO interface, the authors had used the symmetric (LAO)5.0/(STO)5.5 slab with two identical TiO_2/LAO interfaces and a vacuum region between the slab and its periodic image of about 20 Å. The shape and the size of the simulation slab of tetragonal symmetry were unchanged during atomic relaxation, with the in-plane constant of the 2×2 lattice fixed to a = 3.905 Å. The electronic correlation was taken into account by using the GGA+U method in Dudarev's approach,[88] where the on-site Coulomb interaction parameter U was taken to be 4 eV for Ti 3*d*-orbitals and 8 eV for the La 4*f*-orbitals. Additionally, the calculations were performed for the value of U_{Ti} = 7.4 eV (usually used for the correction of the bandgap of STO). The simulations were conducted for the following systems: a) the ideal interface at the presence of a O_2 molecule near the AlO_2-terminated surface to imitate LAO/STO in oxidizing environment; b) the ideal interface with atomic O, placed atop the Al site, modeling oxygen adsorption on the AlO_2-terminated surface; c) the interface with a single Sr ion, removed from the interfacial SrO layer (Sr vacancy) and placed at the central site on top of the AlO_2 surface layer in the near vicinity of the adsorbed O atom, modeling the Sr precipitation on the surface; d) the ideal interface and La–O vacancy in the LaO overlayer at the presence of O_2 molecule nearby; and e) interface with removed Sr, placed at the La site in LaO overlayer together with O at the O vacancy site.

Supporting Information

Supporting Information is available from the Wiley Online Library or from the author.

Acknowledgements

F.G. and M.R. thank the funding of Deutsche Forschungsgemeinschaft (DFG) through DFG GU/1604 (No. 315025796). The PNNL work was supported by the U.S. Department of Energy (DOE), Office of Science, Office of Basic Energy Sciences, Division of Materials Sciences and Engineering under Award #10122. The authors acknowledge the CERIC-ERIC Consortium for the access to experimental facilities and financial support. D.N.M. gratefully acknowledges support by the Juelich Joint Redox Lab (JJRL). This research used resources of the Advanced Light Source (Beamline 11.0.2), a U.S. DOE Office of Science User Facility under contract no. DE-AC02-05CH11231. M.L. and I.S. gratefully acknowledge the funding of Deutsche Forschungsgemeinschaft (DFG) through SFB 917 "Nanoswitches", and the computing time granted through JARA on the supercomputer JURECA,[89] project JIFF38.

Open access funding enabled and organized by Projekt DEAL.

Note: The spelling of the author name Marjana Ležaić was corrected on January 25, 2021, after initial publication online.

Conflict of Interest

The authors declare no conflict of interest.

Keywords

charge-transfer, in situ spectroscopy, mesoscopic transport, oxide heterointerfaces, 2D electron-gases

Received: June 17, 2020
Revised: August 31, 2020
Published online: December 2, 2020

[1] J. Mannhart, D. G. Schlom, *Science* **2010**, *327*, 607.
[2] H. Y. Hwang, Y. Iwasa, M. Kawasaki, B. Keimer, N. Nagaosa, Y. Tokura, *Nat. Mater.* **2012**, *11*, 103.
[3] D. M. Smyth, *The Defect Chemistry of Metal Oxides*, Oxford University Press, Oxford, UK **2000**.
[4] R. Moos, K. H. Härdtl, *J. Am. Ceram. Soc.* **1997**, *80*, 2549.
[5] R. Meyer, A. F. Zurhelle, R. A. De Souza, R. Waser, F. Gunkel, *Phys. Rev. B* **2016**, *94*, 115408.
[6] R. Merkle, J. Maier, *Angew. Chem., Int. Ed.* **2008**, *47*, 3874.
[7] R. Waser, R. Hagenbeck, *Acta Mater.* **2000**, *48*, 797.
[8] P. Zubko, S. Gariglio, M. Gabay, P. Ghosez, J. Triscone, *Annu. Rev. Condens. Matter Phys.* **2011**, *2*, 141.
[9] A. Verma, S. Raghavan, S. Stemmer, D. Jena, *Appl. Phys. Lett.* **2015**, *107*, 192908.
[10] A. Ohtomo, H. Y. Hwang, *Appl. Phys. Lett.* **2004**, *84*, 1716.
[11] F. Gunkel, R. Waser, A. H. H. Ramadan, R. A. De Souza, S. Hoffmann-Eifert, R. Dittmann, *Phys. Rev. B* **2016**, *93*, 245431.
[12] S. Bagdzevicius, K. Maas, M. Boudard, M. Burriel, *J. Electroceram.* **2017**, *39*, 157.
[13] S. Sanna, V. Esposito, J. W. Andreason, J. Hjelm, W. Zhang, T. Kasama, S. B. Simonsen, M. Christensen, S. Linderoth, N. Pryds, *Nat. Mater.* **2015**, *14*, 500.
[14] M. Bibes, J. E. Villegas, A. Barthelemy, *Adv. Phys.* **2011**, *60*, 5.
[15] J. Mannhart, D. H. A. Blank, H. Y. Hwang, A. J. Millis, J.-M. Triscone, *MRS Bull.* **2008**, *33*, 1027.
[16] R. Pentcheva, W. E. Pickett, *Phys. Rev. B* **2006**, *74*, 35112.
[17] R. Pentcheva, W. E. Pickett, *Phys. Rev. B* **2008**, *78*, 205106.
[18] A. Gloter, G. Tieri, D. Li, M. Caputo, V. Strocov, O. Stéphan, J. Triscone, S. Gariglio, *APL Mater.* **2020**, *8*, 041103.
[19] P. Moetakef, J. Y. Zhang, A. Kozhanov, B. Jalan, R. Sehadri, S. J. Allen, S. Stemmer, *Appl. Phys. Lett.* **2011**, *98*, 112110.
[20] P. Moetakef, T. A. Cain, D. G. Ouellette, J. Y. Zhang, D. O. Klenov, A. Janotti, C. G. Van de Walle, S. Rajan, S. J. Allen, S. Stemmer, *Appl. Phys. Lett.* **2011**, *99*, 232116.
[21] A. Ohtomo, H. Y. Hwang, *Nature* **2004**, *427*, 423.
[22] N. Nakagawa, H. Y. Hwang, D. A. Muller, *Nat. Mater.* **2006**, *5*, 204.
[23] M. Huijben, A. Brinkman, G. Koster, G. Rijnders, H. Hilgenkamp, D. H. A. Blank, *Adv. Mater.* **2009**, *21*, 1665.
[24] Y. Z. Chen, F. Trier, T. Wijnands, R. J. Green, N. Gauquelin, R. Egoavil, D. V. Christensen, G. Koster, M. Huijben, N. Bovet, S. Macke, F. He, R. Sutarto, N. H. Andersen, J. A. Sulpizio, M. Honig, G. E. D. K. Prawiroatmodjo, T. S. Jespersen, S. Linderoth, S. Ilani, J. Verbeeck, G. Van Tendeloo, G. Rijnders, G. A. Sawatzky, N. Pryds, *Nat. Mater.* **2015**, *14*, 801.
[25] J. Son, P. Moetakef, B. Jalan, O. Bierwagen, N. J. Wright, R. Engel-Herbert, S. Stemmer, *Nat. Mater.* **2010**, *9*, 482.
[26] S. Gariglio, A. Fête, J. Triscone, *J. Phys.: Condens. Matter* **2015**, *27*, 283201.
[27] N. Reyren, S. Thiel, A. D. Caviglia, L. F. Kourkoutis, G. Hammerl, C. Richter, C. W. Schneider, T. Kopp, A.-S. Ruetschi, D. Jaccard, M. Gabay, D. A. Muller, J. -M. Triscone, J. Mannhart, *Science* **2007**, *317*, 1196.
[28] A. Brinkman, M. Huijben, M. Van Zalk, J. Huijben, U. Zeitler, J. C. Maan, W. G. Van der Wiel, G. Rijnders, D. H. A. Blank, H. Hilgenkamp, *Nat. Mater.* **2007**, *6*, 493.
[29] L. Li, C. Richter, J. Mannhart, R. C. Ashoori, *Nat. Phys.* **2011**, *7*, 762.
[30] D. A. Dikin, M. Mehta, C. W. Bark, C. M. Folkman, C. B. Eom, V. Chandrasekhar, *Phys. Rev. Lett.* **2011**, *107*, 056802.
[31] E. Breckenfeld, N. Bronn, J. Karthik, A. R. Damodaran, S. Lee, N. Mason, L. W. Martin, *Phys. Rev. Lett.* **2013**, *110*, 196804.
[32] F. Gunkel, K. Skaja, A. Shkabko, R. Dittmann, S. Hoffmann-Eifert, R. Waser, *Appl. Phys. Lett.* **2013**, *102*, 71601.
[33] A. Kalabukhov, R. Gunnarsson, J. Borjesson, E. Olsson, T. Claeson, D. Winkler, *Phys. Rev. B* **2007**, *75*, 121404.
[34] C. Xu, C. Baeumer, R. A. Heinen, S. Hoffmann-Eifert, F. Gunkel, R. Dittmann, *Sci. Rep.* **2016**, *6*, 22410.
[35] M. Basletic, J. Maurice, C. Carretero, G. Herranz, O. Copie, M. Bibes, E. Jacquet, K. Bouzehouane, S. Fusil, A. Barthelemy, *Nat. Mater.* **2008**, *7*, 621.
[36] S. Thiel, G. Hammerl, A. Schmehl, C. W. Schneider, J. Mannhart, *Science* **2006**, *313*, 1942.
[37] F. V. E. Hensling, D. J. Keeble, J. Zhu, S. Brose, C. Xu, F. Gunkel, S. Danylyuk, S. S. Nonnenmann, W. Egger, R. Dittmann, *Sci. Rep.* **2018**, *8*, 8846.
[38] F. Gunkel, S. Hoffmann-Eifert, R. Dittmann, S. B. Mi, C. L. Jia, P. Meuffels, R. Waser, *Appl. Phys. Lett.* **2010**, *97*, 12103.
[39] H.-J. Hagemann, H. Ihrig, *Phys. Rev. B* **1979**, *20*, 3871.
[40] R. Hagenbeck, *Simulation der elektrischen Korngrenzeneigenschaften akzeptordotierter $SrTiO_3$-Keramiken*, RWTH Publications, Aachen, Germany **1999**.
[41] T. Tanaka, K. Matsunaga, Y. Ikuhara, T. Yamamoto, *Phys. Rev. B* **2003**, *68*, 205213.
[42] R. Waser, *J. Am. Ceram. Soc.* **1991**, *74*, 1934.
[43] M. Riva, G. Franceschi, Q. Lu, M. Schmid, B. Yildiz, U. Diebold, *Phys. Rev. Mater.* **2019**, *3*, 43802.
[44] M. Andrä, F. Dvorák, M. Vorokhta, S. Nemšák, V. Matolín, C. M. Schneider, R. Dittmann, F. Gunkel, D. N. Mueller, R. Waser, *APL Mater.* **2017**, *5*, 56106.
[45] M. Andrae, H. Bluhm, C. M. Schneider, R. Dittmann, R. Waser, D. N. Mueller, F. Gunkel, *Phys. Rev. Mater.* **2019**, *3*, 44604/1.
[46] A. D. Caviglia, S. Gariglio, C. Cancellieri, B. Sacepe, A. Fete, N. Reyren, M. Gabay, A. F. Morpurgo, J.-M. Triscone, *Phys. Rev. Lett.* **2010**, *105*, 236802.
[47] M. Ben Shalom, A. Ron, A. Palevski, Y. Dagan, *Phys. Rev. Lett.* **2010**, *105*, 206401.
[48] F. Gunkel, S. Wicklein, P. Brinks, S. Hoffmann-Eifert, M. Huijben, G. Rijnders, R. Waser, R. Dittmann, *Nanoscale* **2015**, *7*, 1013.
[49] A. Joshua, S. Pecke, J. Ruhman, E. Altman, S. Ilani, *Nat. Commun.* **2012**, *3*, 1129.
[50] F. Gunkel, C. Bell, H. Inoue, B. Kim, A. G. Swartz, T. A. Merz, Y. Hikita, S. Harashima, H. K. Sato, M. Minohara, S. Hoffmann-Eifert, R. Dittmann, H. Y. Hwang, *Phys. Rev. X* **2016**, *6*, 031035.
[51] D. Stornaiuolo, C. Cantoni, G. M. De Luca, R. Di Capua, E. Di Gennaro, G. Ghiringhelli, B. Jouault, D. Marre, D. Massarotti, F. M. Granozio, I. Pallecchi, C. Piamonteze, S. Rusponi, F. Tafuri, M. Salluzzo, *Nat. Mater.* **2016**, *15*, 278.
[52] D. Doennig, R. Pentcheva, *Sci. Rep.* **2015**, *5*, 7909.
[53] W. Jiang, X. Z. Zhou, G. Williams, *Phys. Rev. B* **2010**, *82*, 144424.
[54] S. X. Zhang, W. Yu, S. B. Ogale, S. R. Shinde, D. C. Kundaliya, W. Tse, S. Y. Young, J. S. Higgins, L. G. Salamanca-Riba, M. Herrera, L. F. Fu, N. D. Browning, R. L. Greene, T. Venkatesan, *Phys. Rev. B* **2007**, *76*, 085323.
[55] R. Mathieu, A. Asamitsu, H. Yamada, K. S. Takahashi, M. Kawasaki, Z. Fang, N. Nagaosa, Y. Tokura, *Phys. Rev. Lett.* **2004**, *93*, 016602.
[56] D. V. Christensen, Y. Frenkel, P. Schuetz, F. Trier, S. Wissberg, R. Claessen, B. Kalisky, A. Smith, Y. Chen, N. Pryds, *Phys. Rev. Appl.* **2018**, *9*, 054004.
[57] A. Sarantopoulos, E. Ferreiro-Vila, V. Pardo, C. Magen, M. H. Aguirre, F. Rivadulla, *Phys. Rev. Lett.* **2015**, *115*, 166801.
[58] O. Copie, V. Garcia, C. Boedefeld, C. Carretero, M. Bibes, G. Herranz, E. Jacquet, J. Maurice, B. Vinter, S. Fusil, K. Bouzehouane, H. Jaffres, A. Barthelemy, *Phys. Rev. Lett.* **2009**, *102*, 216804.
[59] J. M. Pan, B. L. Maschhoff, U. Diebold, T. E. Madey, *J. Vac. Sci. Technol. A* **1992**, *10*, 2470.
[60] K. Szot, W. Speier, U. Breuer, R. Meyer, J. Szade, R. Waser, *Surf. Sci.* **2000**, *460*, 112.

[61] P. A. W. van der Heide, Q. D. Jiang, Y. S. Kim, J. W. Rabalais, *Surf. Sci.* **2001**, *473*, 59.
[62] U. Treske, N. Heming, M. Knupfer, B. Buechner, A. Koitzsch, E. Di Gennaro, U. S. di Uccio, F. Miletto Granozio, S. Krause, *APL Mater.* **2014**, *2*, 12108.
[63] S. A. Chambers, Y. Du, Z. Zhu, J. Wang, M. J. Wahila, L. F. J. Piper, A. Prakash, J. Yue, B. Jalan, S. R. Spurgeon, D. M. Kepaptsoglou, Q. M. Ramasse, P. V. Sushko, *Phys. Rev. B* **2018**, *97*, 245204.
[64] L. Wang, Y. Du, L. Chang, K. A. Soerzinger, M. E. Bowden, J. Wang, S. A. Chambers, *Appl. Phys. Lett.* **2018**, *112*, 261601.
[65] E. Slooten, Ph.D. Thesis, University of Amsterdam, Amsterdam, The Netherlands **2013**.
[66] U. Treske, N. Heming, M. Knupfer, B. Büchner, E. Di Gennaro, A. Khare, U. S. Di Uccio, F. M. Granozio, S. Krause, A. Koitzsch, *Sci. Rep.* **2015**, *5*, 14506.
[67] Y. Segal, J. H. Ngai, J. W. Reiner, F. J. Walker, C. H. Ahn, *Phys. Rev. B* **2009**, *80*, 241107.
[68] S. A. Chambers, M. H. Engelhard, V. Shutthanandan, Z. Zhu, T. C. Droubay, L. Qiao, P. V. Sushko, T. Feng, H. D. Lee, T. Gustafsson, E. Garfunkel, A. B. Shah, J.-M. Zuo, Q. M. Ramasse, *Surf. Sci.* **2010**, *65*, 317.
[69] E. Slooten, Z. Zhong, H. J. A. Molegraaf, P. D. Eerkes, S. de Jong, F. Massee, E. van Heumen, M. K. Kruize, S. Wenderich, J. E. Kleibeuker, M. Gorgoi, H. Hilgenkamp, A. Brinkman, M. Huijben, G. Rijnders, D. H. A. Blank, G. Koster, P. J. Kelly, M. S. Golden, *Phys. Rev. B* **2013**, *87*, 85128.
[70] G. Drera, G. Salvinelli, A. Brinkman, M. Huijben, G. Koster, H. Hilgenkamp, G. Rijnders, D. Visentin, L. Sangaletti, *Phys. Rev. B* **2013**, *87*, 75435.
[71] L. Yu, A. Zunger, *Nat. Commun.* **2014**, *5*, 5118.
[72] C. Lenser, A. Koehl, I. Slipukhina, H. Du, M. Patt, V. Feyer, C. M. Schneider, M. Lezaic, R. Waser, R. Dittmann, *Adv. Funct. Mater.* **2015**, *25*, 6360.
[73] F. Gunkel, P. Brinks, S. Hoffmann-Eifert, R. Dittmann, M. Huijben, J. E. Kleibeuker, G. Koster, G. Rijnders, R. Waser, *Appl. Phys. Lett.* **2012**, *100*, 52103.
[74] V. N. Strocov, A. Chikina, M. Caputo, M.-A. Husanu, F. Bisti, D. Bracher, T. Schmitt, F. Miletto Granozio, C. A. F. Vaz, F. Lechermann, *Phys. Rev. Mater.* **2019**, *3*, 106001.
[75] N. Mohanta, A. Taraphder, *J. Phys.: Condens. Matter* **2014**, *26*, 025705.
[76] D. J. Keeble, S. Wicklein, L. Jin, C. L. Jia, W. Egger, R. Dittmann, *Phys. Rev. B* **2013**, *87*, 11.
[77] M. P. Warusawithana, C. Richter, J. A. Mundy, P. Roy, J. Ludwig, S. Paetel, T. Heeg, A. A. Pawlicki, L. F. Kourkoutis, M. Zheng, M. Lee, B. Mulcahy, W. Zander, Y. Zhu, J. Schubert, J. N. Eckstein, D. A. Muller, C. S. Hellberg, J. Mannhart, D. G. Schlom, *Nat. Commun.* **2013**, *4*, 2351.
[78] F. Gunkel, S. Hoffmann-Eifert, R. A. Heinen, D. V. Christensen, Y. Z. Chen, N. Pryds, R. Waser, R. Dittmann, *ACS Appl. Mater. Interfaces* **2017**, *9*, 1086.
[79] H. K. Sato, C. Bell, Y. Hikita, H. Y. Hwang, *Appl. Phys. Lett.* **2013**, *102*, 251602.
[80] T. L. Meyer, H. Jeen, X. Gao, J. R. Petrie, M. F. Chisholm, H. N. Lee, *Adv. Electron. Mater.* **2016**, *2*, 1500201/1.
[81] D. F. Ogletree, H. Bluhm, E. D. Hebenstreit, M. Salmeron, *Nucl. Instrum. Methods Phys. Res. Sect. A* **2009**, *601*, 151.
[82] R. Moos, W. Menesklou, K. H. Hardtl, *Appl. Phys. A* **1995**, *61*, 389.
[83] G. Kresse, J. Furthmüller, *Comput. Mater. Sci.* **1996**, *6*, 15.
[84] G. Kresse, J. Furthmüller, *Phys. Rev. B* **1996**, *54*, 11169.
[85] G. Kresse, J. Hafner, *Phys. Rev. B* **1993**, *47*, 558.
[86] J. P. Perdew, K. Burke, M. Ernzerhof, *Phys. Rev. Lett.* **1996**, *77*, 3865.
[87] P. E. Blöchl, *Phys. Rev. B* **1994**, *50*, 17953.
[88] S. Dudarev, G. Botton, S. Savrasov, C. Humphreys, A. Sutton, *Phys. Rev. B* **1998**, *57*, 1505.
[89] D. Krause, P. Thörnig, *J. Large-Scale Res. Facil.* **2018**, *4*, A132.